Neutrino Signatures from Young Neutron Stars

60

Luke F. Roberts and Sanjay Reddy

Abstract

After a successful core collapse supernova (CCSN) explosion, a hot dense proto-neutron star (PNS) is left as a remnant. Over a time of 20 or so seconds, this PNS emits the majority of the neutrinos that come from the CCSN, contracts, and loses most of its lepton number. This is the process by which all neutron stars in our galaxy are likely born. The emitted neutrinos were detected from supernova (SN) 1987A, and they will be detected in much greater numbers from any future galactic CCSN. These detections can provide a direct window into the properties of the dense matter encountered inside neutron stars, and they can affect nucleosynthesis in the material ejected during the CCSN. In this chapter, we review the basic physics of PNS cooling, including the basic equations of PNS structure and neutrino diffusion in dense matter. We then discuss how the nuclear equation of state, neutrino opacities in dense matter, and convection can shape the temporal behavior of the neutrino signal. We also discuss what was learned from the late-time SN 1987A neutrinos, the prospects for detection of these neutrinos from future galactic CCSNe, and the effects these neutrinos can have on nucleosynthesis.

L.F. Roberts (✉)
Theoretical AstroPhysics Including Relativity and Cosmology (TAPIR), California Institute of Technology, Pasadena, CA, USA
e-mail: lroberts@tapir.caltech.edu

S. Reddy
Institute for Nuclear Theory, University of Washington, Seattle, WA, USA
e-mail: sareddy@uw.edu

A.W. Alsabti, P. Murdin (eds.), *Handbook of Supernovae*,
https://doi.org/10.1007/978-3-319-21846-5_5

Contents

1 Introduction

A nascent neutron star (NS) is often left as the remnant of a successful core collapse supernova (CCSN). This young NS emits a copious number of neutrinos over the first few seconds of its life. During this time it is referred to as a proto-neutron star (PNS). Due to the high densities and temperatures encountered inside the PNS, neutrinos cannot freely escape but instead must diffuse out over a period of about a minute (Burrows and Lattimer 1986). This neutrino emission is powered by a large fraction of the gravitational binding energy released by taking the iron core of a massive star and transforming it into a NS ($2–5 \times 10^{53}$ erg s) (Baade and Zwicky 1934). After about a minute, neutrinos can escape freely, which demarcates the transition from PNS to NS. This qualitative picture of late PNS neutrino emission was confirmed when about thirty neutrinos were observed from supernova (SN) 1987A over a period of about 15 s (Bionta et al. 1987; Hirata et al. 1987). If a CCSN were observed in our galaxy today, modern neutrino detectors would see thousands of events (Scholberg 2012). The neutrino signal is shaped by the nuclear equation of state (EoS) and neutrino opacities. Therefore, detection of galactic CCSN neutrinos would give a detailed window into the birth of NSs and the properties of matter at and above nuclear density.

In addition to direct neutrino detection, there are other reasons why understanding the properties of these late-time CCSN neutrinos is important. First, they can influence nucleosynthesis in CCSNe (Woosley et al. 1990). In particular, PNS neutrino emission almost wholly determines what nuclei are synthesized in baryonic material blown off the surface of PNSs (Hoffman et al. 1997; Roberts et al. 2010; Woosley et al. 1994). Second, the integrated neutrino emission from CCSNe receives a large contribution from PNS neutrinos. Therefore, accurate models of PNS neutrino emission can contribute to understanding the diffuse SN neutrino background (Nakazato et al. 2015). Finally, the neutrino emission from the "neutrinosphere" of PNSs gives the initial conditions for the study of both

matter-induced and neutrino-induced neutrino oscillations (Duan et al. 2006). The rate of PNS cooling also has the potential to put limits on exotic physics and possible extensions of the standard model using data already in hand from SN 1987A (Keil et al. 1997; Pons et al. 2001a,b).

In this chapter, we discuss PNS cooling and the late-time CCSN neutrino signal. In Sect. 2, we focus on the basic equations of PNS cooling (Sect. 2.1) and models of PNS cooling (Sects. 2.2 and 2.4). In Sect. 3, we discuss the various ingredients that shape the CCSN neutrino signal, the nuclear equation of state, neutrino opacities, and convection, respectively. Finally – in Sects. 4.1, 4.2, and 4.3 – we discuss the observable consequences of late-time CCSN neutrinos. Throughout the chapter, we set $\hbar = c = 1$.

2 PNS Cooling

Essentially, all of the energy that powers the neutrino emission during a CCSN comes from the gravitational binding energy released when taking the white dwarf like iron core of the massive progenitor star and turning it into a NS (Baade and Zwicky 1934), which is

$$E_{\rm SN} \sim \frac{3GM_{\rm pns}^2}{5r_{\rm NS}} \approx 3 \times 10^{53}\,{\rm erg} \left(\frac{M_{\rm pns}}{{\rm M}_\odot}\right)^2 \left(\frac{r_{NS}}{12\,{\rm km}}\right)^{-1}. \quad (1)$$

The CCSN shock forms at an enclosed mass of $\sim$0.4 $\mathrm{M}_\odot$ and the material that is shock heated increases the effective PNS radius. This provides a reservoir of gravitational potential energy that can be converted into neutrinos. Therefore, around two thirds of the total energy, $E_{\rm SN}$, is available during the PNS cooling phase.

After the CCSN shock has passed through the PNS, the interior entropy varies between one and six k_b/baryon. Peak temperatures between 30 and 60 MeV are reached during PNS evolution, while the surface of the PNS has a temperature around 3–5 MeV. The interior of the PNS is comprised of interacting protons, neutrons, and electrons, at densities greater than a few times nuclear saturation density ($\rho_s \approx 2.8 \times 10^{14}\,{\rm g\,cm^{-3}}$) toward the center of the PNS. It is also possible that more exotic degrees of freedom are present in the inner most regions of the PNS (Prakash et al. 1997).

During core collapse, electron capture on heavy nuclei removes around 40 % of the electrons from the core before neutrinos become trapped (Hix et al. 2003), leaving behind $Y_e \approx 0.3$ in the core. Y_e is the number of electrons per baryon and is equal to the proton fraction by charge conservation. Although this constitutes a large portion of the initial lepton number of the core, a cold NS has an even lower total lepton number. The lepton number of the PNS is the total number of electrons plus electron neutrinos minus the number of positrons and electron antineutrinos, which is a conserved quantity. In a cold NS, the interactions $e^- + p \rightarrow \nu_e + n$ and $n \rightarrow \bar{\nu}_e + e^- + p$ are in equilibrium. Equating these rates and solving for the

electron fraction result in $Y_e \sim 0.1$ for the densities encountered in the cores of NSs. Therefore, the PNS must "deleptonize" to become a NS, which requires losing a total lepton number of around

$$N_L \approx 3.4 \times 10^{56} \left(\frac{M_{\rm pns}}{1.4\,{\rm M}_\odot} \right), \tag{2}$$

which must be removed from the PNS by neutrinos.

Inside the PNS, a copious number of neutrinos of all flavors are produced and scattered by weak interactions involving both the baryons and the leptons present in the medium. The rate at which neutrinos leave the PNS and carry off energy and lepton number will depend on thermal neutrino mean free path inside the PNS with energy $\varepsilon_\nu \sim 60\,{\rm MeV}$. Using a reference weak interaction neutrino cross section (see Sect. 3.1),

$$\sigma_\nu = \frac{4 G_F^2 \varepsilon_\nu^2}{\pi} \approx 3 \times 10^{-40}\,{\rm cm}^2 \left(\frac{\varepsilon_\nu}{60\,{\rm MeV}} \right)^2, \tag{3}$$

where G_F is the Fermi coupling constant and ε_ν is the neutrino energy. A naive estimate of the neutrino mean free path in the PNS is then

$$\lambda_\nu \sim \frac{1}{\bar{n}_b \sigma_\nu} \approx 14\,{\rm cm} \left(\frac{\bar{\varepsilon}_\nu}{60\,{\rm MeV}} \right)^{-2} \left(\frac{R_{\rm pns}}{12\,{\rm km}} \right)^3 \left(\frac{M_{\rm pns}}{{\rm M}_\odot} \right)^{-1}, \tag{4}$$

where $\bar{n}_b = 3 M_{\rm pns}/(4\pi R_{\rm pns}^3 m_b)$ is the average baryon density of the PNS and $\bar{\varepsilon}_\nu$ is a characteristic energy for neutrinos inside the PNS. The neutrino mean free path is much smaller than the radius of the PNS, which is around 12 km once the shock-heated mantle has cooled. Therefore, neutrinos must escape from the PNS diffusively and will be in thermal and chemical equilibrium with the baryons and electrons throughout most of the PNS.

2.1 The Equations of PNS Cooling

Generally, PNS evolution is a neutrino radiation hydrodynamic problem where general relativity is important. A number of simplifications to the general system of equations can be made. First, the PNS cooling timescale is much longer than the sound crossing time of the PNS. Therefore, PNSs are very close to being in hydrostatic equilibrium and spherical symmetric. With these approximations, the equations of PNS cooling become (see Burrows and Lattimer (1986); Pons et al. (1999); Roberts (2012) for detailed derivations)

$$\frac{dP}{dr} = -\frac{G(M_g + 4\pi r^3 P)(\rho + P)}{r^2 \Gamma^2} \tag{5}$$

$$\frac{dM_g}{dr} = 4\pi r^2 \rho \tag{6}$$

$$\frac{dN}{dr} = \frac{4\pi r^2 n_b}{\Gamma} \tag{7}$$

$$\frac{d\alpha}{dP} = -\frac{\alpha}{P+\rho} \tag{8}$$

$$\frac{dY_L}{dt} = -\frac{\partial(4\pi\alpha r^2 F_L)}{\partial N} \tag{9}$$

$$\frac{dY_e}{dt} = \alpha\frac{S_N}{n_b} \tag{10}$$

$$\frac{d((\rho+\rho_\nu)/n_b)}{dt} = -\alpha^{-1}\frac{\partial(4\pi\alpha^2 r^2 H_\nu)}{\partial N} - (P+P_\nu)\frac{d(1/n)}{dt} \tag{11}$$

$$\frac{d(\rho/n_b)}{dt} = \alpha\frac{S_E}{n_b} - P\frac{d(1/n)}{dt}. \tag{12}$$

Equations 5, 6, 7, and 8 are just the relativistic equations of hydrostatic equilibrium, where P is the pressure, ρ is the energy density of the background fluid, ρ_ν is the energy density of the neutrinos, n_b is the baryon density, M_g is the gravitational mass, N is the enclosed baryon number, r is the radius, $\Gamma = \sqrt{1-2GM_g/r}$, and α is the lapse function. The lepton fraction is $Y_L = Y_e + Y_{\nu_e}$, where Y_e is the number of electron per baryon and $Y_{\nu_e} = (n_{\nu_e} - n_{\bar{\nu}_e})/n_b$ is the local net number of electron neutrinos per baryon. Equations 9 and 11 describe the conservation of lepton number and total internal energy in the PNS. Throughout most of the PNS, Eqs. 10 and 12 are zero and can be neglected since the neutrino number and energy source functions, S_N and S_E, rapidly bring the neutrinos into thermal equilibrium with the background fluid. The energy flux and lepton number fluxes are given by $F_L = F^N_{\nu_e} - F^N_{\bar{\nu}_e}$ and $H_\nu = \sum F^E_i$ (where the sum runs over all flavors of neutrinos and antineutrinos). The number and energy fluxes of individual neutrino species are given by

$$F^{\{N\}}_{\nu_i} = \frac{2\pi}{(2\pi)^3}\int_0^\infty d\varepsilon\varepsilon^{\{2\}}\int_{-1}^1 d\mu\mu f_{\nu_i}, \tag{13}$$

where $f_{\nu_i} = f_{\nu_i}(t, r, \varepsilon, \mu)$ is the distribution function of neutrinos of species i, μ is the cosine of the angle of neutrino propagation relative to the radial direction, and ε is the neutrino energy. Below, we often discuss the neutrino luminosity $L_{\nu_i} = 4\pi r^2\alpha^2 F^E_i$ and the neutrino number luminosity $\dot{N}_{\nu_i} = 4\pi r^2\alpha F^N_i$.

The solution of this system of equations requires a method of determining the f_{ν_i}, the evolution of which is determined by the Boltzmann equation:

$$\frac{Df_{\nu_i}}{Dl} = (\eta_{a,i} + \eta_{s,i}[f_{\nu_i}])(1-f_{\nu_i}) - (\kappa_{a,i} + \kappa_{s,i}[f_{\nu_i}])f_{\nu_i}, \tag{14}$$

where D/Dl is a Lagrangian derivative in phase space, eta_a and η_s are absorption–scattering emissivities, and κ_a and κ_s are absorption and scattering opacities (Lindquist 1966; Thorne 1981). The evolution of the f_ν can be attacked directly with the Boltzmann equation, but neutrino transport simplifies greatly throughout most of the PNS. As was mentioned above, the neutrino mean free path inside the PNS is much shorter than the distance over which n_b, T, and Y_e are changing. Therefore, the neutrino distribution functions are very close to thermal and the neutrinos propagate through the star diffusively. In the diffusion limit of the Boltzmann equation, the number and energy flux of neutrinos of species i are given by opacity-weighted radial derivatives of the neutrino density (Burrows and Lattimer 1986; Pons et al. 1999):

$$F_{\nu i}^{\{E}^{N\}} = -\frac{\Gamma}{\alpha^{\{4}_{3\}}} \int_0^\infty d\omega \frac{\omega^{\{3}_{2\}}}{3\left(\kappa_{a,i}^* + \kappa_{s,i}^*\right)} \frac{\partial f_{i,\mathrm{FD}}(\omega/\alpha)}{\partial r}, \tag{15}$$

where $f_{i,\mathrm{FD}}(\varepsilon) = [1+\exp(\varepsilon/T-\eta_i)]^{-1}$ is the Fermi–Dirac distribution for neutrinos of species i with degeneracy parameter η_i and ω is the neutrino energy at infinity. Both electron neutrinos and antineutrinos rapidly reach chemical equilibrium with the nuclear medium via charged-current neutrino interactions. Therefore, the electron neutrino chemical potential is $\mu_{\nu_e} = \mu_e + \mu_p - \mu_n$ and $\mu_{\bar{\nu}_e} = -\mu_{\nu_e}$. Because of the large mass of the μ and τ particles, no net μ or τ number is produced in the PNS and $\mu_{\nu_\mu} = \mu_{\nu_\tau} = 0$. The quantity $\kappa_{a,i}^*$ is the total absorption opacity corrected for detailed balance and $\kappa_{s,i}^*$ is the scattering transport opacity (Burrows et al. 2006; Pons et al. 1999). These opacities have units of inverse length and are approximately $\kappa \sim n_b \sigma_\nu$. In the equilibrium diffusion limit, the isotropic parts of the neutrino distribution functions only depend on the local temperature, as well as the electron neutrino degeneracy factor, $\eta_{\nu_e} = \mu_{\nu_e}/T$, for electron neutrinos and antineutrinos. The chemical potentials of the μ and τ neutrinos are zero throughout the PNS due to the large masses of the μ and τ particles. With these assumptions, the total lepton and energy fluxes in the diffusion limit become

$$F_L = -\frac{\Gamma T^2}{\alpha 6\pi^2}\left[D_3 \frac{\partial(\alpha T)}{\partial r} + D_2 \alpha T \frac{\partial \eta_{\nu_e}}{\partial r}\right] \tag{16}$$

$$H_\nu = -\frac{\Gamma T^3}{\alpha 6\pi^2}\left[D_4 \frac{\partial(\alpha T)}{\partial r} + D_3 \alpha T \frac{\partial \eta_{\nu_e}}{\partial r}\right], \tag{17}$$

where $D_2 = D_2^{\nu_e} + D_2^{\bar{\nu}_e}$, $D_3 = D_3^{\nu_e} - D_3^{\bar{\nu}_e}$, and $D_4 = \sum_i D_4^i$ are diffusion coefficients. The single-species diffusion coefficients are Rosseland mean opacities defined by

$$D_n^i = \int_0^\infty d\varepsilon \frac{\varepsilon^n f_{i,\mathrm{FD}}(1 - f_{i,\mathrm{FD}})}{T^{n+1}\left(\kappa_{a,i}^* + \kappa_{s,i}^*\right)}. \tag{18}$$

Only electron neutrinos and antineutrinos contribute to the lepton flux diffusion coefficients, while all species contribute to the energy flux diffusion coefficients. Note that the diffusion coefficients will be $\sim \lambda_\nu(\langle\varepsilon_\nu\rangle)$, where $\langle\varepsilon_\nu\rangle$ is an average neutrino energy in the medium. This makes it clear that gradients in the temperature and μ_{ν_e} in the PNS core, combined with the neutrino opacities, drive its deleptonization and cooling.

In addition to these structure and transport equations, a model for the dense matter encountered in the PNS, as well as the initial configuration of s and Y_L versus radius, is required to predict the PNS neutrino signal. The EoS – which determines ρ, P, and μ_{ν_e} as a function of n_b, T, and Y_e – and the neutrino diffusion coefficients depend strongly on the properties of matter at and above nuclear saturation density.

The equilibrium diffusion equations described above provide an excellent approximation to neutrino transport in the optically thick interior regions of the PNS, are useful for understanding the basic properties of PNS cooling, and have been used – along with flux limiters to prevent superluminal transport of energy and lepton number (Burrows and Lattimer 1986) – in numerous works studying the cooling of PNSs (Burrows and Lattimer 1986; Keil and Janka 1995; Pons et al. 1999; Roberts et al. 2012). Nonetheless, they are not suited to describe the neutrino transport near the surface where the neutrino mean free paths become large. They also cannot provide any information about the average energies of the neutrinos that emerge from the neutron star since they assume neutrinos are everywhere in thermal equilibrium with the background material. Therefore, some works have employed nonequilibrium, spectral neutrino transport at varying levels of sophistication (Fischer et al. 2010; Hüdepohl et al. 2010; Nakazato et al. 2013; Roberts et al. 2012; Sumiyoshi et al. 1995; Woosley et al. 1994). These methods all evolve the nonequilibrium distribution function of the neutrinos, f_{ν_i}, at a large number of neutrino energies using the Boltzmann equation or some approximation thereof.

2.2 PNS Evolution

Here, the evolution of a fiducial 1.42 $M_\odot$ PNS model is described. PNS evolution has been modeled using numerical codes for almost 30 years (Burrows 1987; Burrows and Lattimer 1986; Fischer et al. 2010; Hüdepohl et al. 2010; Keil and Janka 1995; Keil et al. 1995; Nakazato et al. 2013; Pons et al. 1999, 2001a; Roberts 2012; Roberts et al. 2012; Sumiyoshi et al. 1995). Although the fidelity to the underlying micro- and macrophysics has improved with time, the basic features of PNS cooling are still the same. The illustrative model discussed in this section was calculated using the multi-energy group neutrino transport method described in Roberts et al. (2012). Even so, throughout most of the PNS this more realistic transport method reduces to the diffusion equations described above.

This calculation began with a pre-SN model of a 15 $M_\odot$ star from Woosley and Weaver (1995). The evolution through core collapse, bounce, and the cessation of shock expansion was followed. Once the SN shock crossed an enclosed baryonic

mass of $1.42\,M_\odot$, the material outside this region was excised from the grid to crudely simulate the CCSN explosion. Then this PNS core was evolved for 100 s. This model is comparable to models found in Hüdepohl et al. (2010) and Fischer et al. (2010). We used an EoS similar to the Lattimer-Swesty equation of state with incompressibility $K_s = 220$ MeV (Lattimer and Douglas Swesty 1991), and all neutrino-nucleon interactions were treated in the elastic limit. The evolution of the interior structure of the model is shown in Fig. 1. The time evolution of various quantities in the center of the PNS as well as its energy and lepton number losses is shown in Fig. 2. These figures also show the evolution of the star during the pre-explosion phase of the SN (see the ▸ Chap. 59, "Neutrino Emission from Supernovae" for a detailed discussion of the early-time emission).

The initial structure left behind after deleptonization during core collapse and shock propagation through the core can be seen with the yellow lines in the panels showing the entropy and the lepton fraction in Fig. 1. There is a low entropy, high lepton number *core* and a high entropy, low lepton number *mantle*. The transition point between these two phases is near the maximum temperature point in the PNS. After collapse and bounce, the SN shock formed near this transition point, so the mantle is shock heated and the core is not. The high entropy found in the mantle increases its pressure and thereby increases its radius and decreases its density relative to the core.

The initial core lepton fraction, $Y_L = 0.33$, is set by the point during core collapse when neutrinos become trapped, which occurs when the core reaches a density near $10^{-4}\,\mathrm{fm}^{-3}$ (Hix et al. 2003). This can be seen in the second and fourth panels of Fig. 2. Electron neutrinos are able to rapidly remove lepton number from the mantle, so this region has $\eta_{\nu_e} \approx 0$.

Once the SN shock begins to explode the star and accretion slows down or ceases, PNS neutrino emission proceeds in three phases: the mantle contraction phase, the deleptonization phase, and the thermal cooling phase. The basic features of these different phases can be seen in Figs. 1 and 2.

Mantle Contraction – During the first few seconds, the neutrino emission is dominated by contributions from the contracting mantle. This contraction is not dynamical. Rather, it is driven by the reduction in pressure due to entropy and electron losses. As can be seen in the second to last panel of Fig. 2, the radius of the PNS contracts from around 100 km to a value very close to the cold NS radius – which is 12 km for the EoS state used in this model – within the first 2 s of PNS evolution. The neutrino luminosity emerging from the surface of the PNS is sourced completely in this region; see the top left panel of Fig. 1. In fact, energy is also being lost from the inner boundary of the mantle as electron antineutrinos and heavy-flavored neutrinos diffuse down the positive temperature gradient into the core; the total neutrino luminosity becomes negative at the core–mantle boundary. Additionally, the deleptonization wave pushes inward over this period but does not reach the center of the PNS. This can be seen in the panels of Fig. 1 showing Y_L and η_{ν_e}.

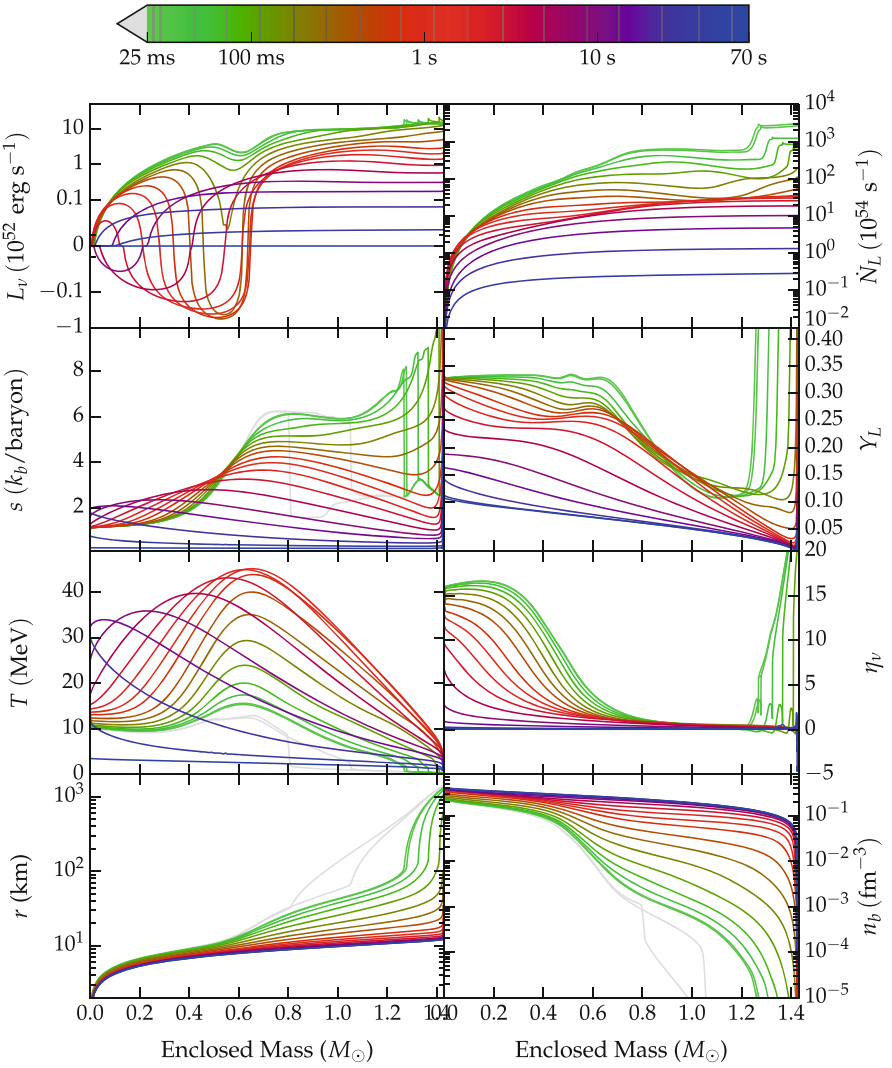

Fig. 1 Interior PNS quantities at selected times, with time coded by color. The semitransparent lines on the color bar demarcate the time of the various lines shown in the panels below it. The *gray lines* are for selected times during the dynamical post-bounce evolution. Here, we focus on the evolution of the inner core after the dynamical phase has ended. The *top left panel* shows the energy carried by all flavors of neutrinos, while the *top right panel* shows the net lepton number transported by neutrinos as a function of enclosed baryonic mass. The *second row of panels* shows the evolution of the entropy and lepton fraction, which is determined by the neutrino fluxes. The *third row of panels* shows the temperature and neutrino degeneracy parameter evolution. Gradients in these quantities drive the diffusive neutrino fluxes. The *final row of panels* shows the radius and baryon density as a function of enclosed baryonic mass to illustrate how the structure of the PNS evolves and contracts in response to loss of energy and lepton number

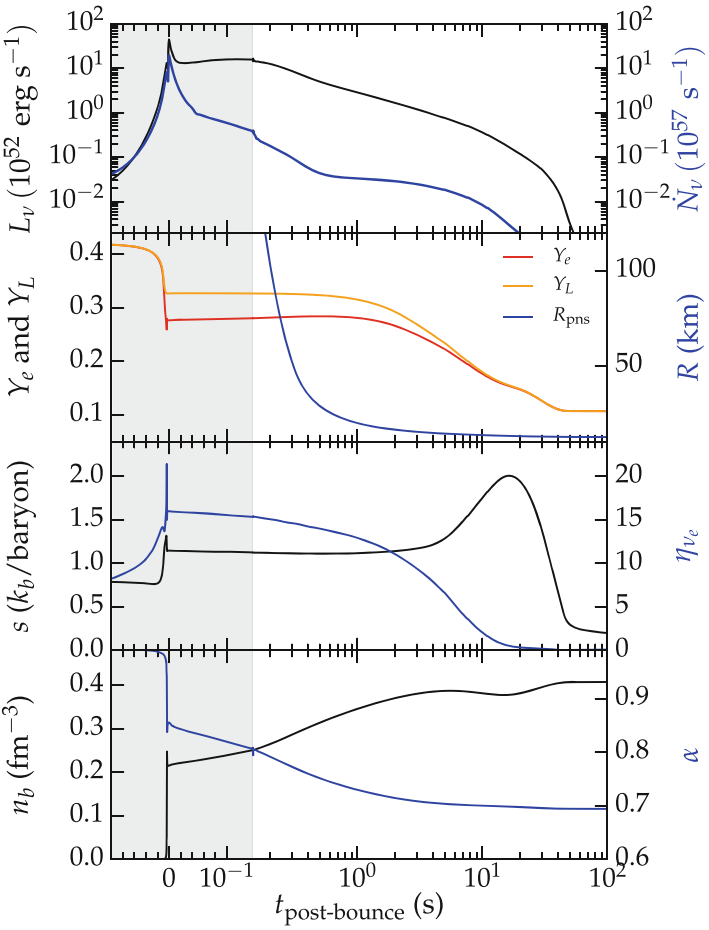

Fig. 2 Time evolution of central quantities and the total neutrino luminosity and lepton flux. The *gray region* corresponds to the accretion phase and is on a linear timescale, while the region to the right is the PNS cooling phase and it is plotted on a logarithmic scale. At the transition from the accretion phase to the PNS cooling phase, all of the material from above the shock is excised from the grid, causing a slight jump in some quantities. The *top panel* shows the total energy loss rate from the PNS and the deleptonization rate. The *second panel* shows the evolution of the central lepton fraction and electron fraction, as well as the PNS radius. The deleptonization era corresponds to the period over which Y_e and Y_L differ. The *third panel* shows the evolution of the central neutrino chemical potential and entropy. The impact of Joule heating is visible between 5 and 20 s. The *bottom panel* shows the central density and the central lapse, α, to illustrate the contraction of the PNS over time

Deleptonization Phase – Once the PNS has settled down too close to the radius of a cold NS, the luminosity evolution is driven by the deleptonization wave that propagates into the center of the PNS and eventually brings the entire PNS to a state where $\eta_{\nu_e} = 0$. This occurs over a period of about 20 s. The lepton number flux is produced by the negative gradient in η_{ν_e} left after the shock breakout in the region between the homologous core and the base of the mantle.

During this period the core entropy and temperature increase, as can be seen in the bottom panel of Fig. 2. This is due to two effects. First, as was the case during the mantle contraction phase, electron antineutrinos and heavy-flavor neutrinos are diffusing inward and heating the core. Second, lepton number is being lost from the core due to the positive flux of electron neutrinos throughout the PNS, which causes "Joule heating" (Burrows and Lattimer 1986). To see this, we recast Eq. 11 in terms of the entropy using the first law of thermodynamics:

$$T\frac{ds}{dt} = -\alpha^{-1}\frac{\partial(4\pi\alpha^2 r^2 H_\nu)}{\partial N} - \mu_{\nu_e}\frac{dY_L}{dt}. \tag{19}$$

Here, s is the entropy per baryon in units of Boltzmann's constant, T is the temperature, and μ_{ν_e} is the electron neutrino chemical potential. Joule heating comes from the second term on the right-hand side of this equation, since $dY_L/dt < 0$ and $\mu_{\nu_e} > 0$. Eventually, the combined effects of these two processes raise the central entropy from around one to two k_b/baryon and create a negative entropy and temperature gradients throughout the star.

Thermal Cooling Phase – Once $\eta_{\nu_e} \sim 0$ throughout the star (see Fig. 1), the PNS slowly contracts as energy leaks from the entire star. Both the entropy and lepton number of the core fall during this period, as shown in Fig. 2. The deleptonization rate falls off rapidly, but it does not go to zero because the local equilibrium electron fraction decreases with the local temperature, so low-level deleptonization continues. The period of PNS cooling ends when the object becomes optically thin to neutrinos and the neutrino luminosity falls off abruptly.

2.3 Analytic Estimates of Cooling Phase Timescales

It is instructive to use the equations of Sect. 2.1 and a few simplifying assumptions to obtain analytic solutions to the neutrino transport equations. This can elucidate how the timescales of the deleptonization and thermal cooling phases depend on the neutrino opacities and the EoS.

At the onset of deleptonization, electron neutrinos are degenerate. Under these conditions, the gradient in neutrino chemical potential dominates the lepton number flux in Eq. 9. Further, due to Pauli blocking, only neutrinos at the Fermi surface contribute, and the relevant diffusion coefficient reduces to

$$D_2 \simeq \frac{\mu_{\nu_e}^2}{2T^2}\,\frac{1}{\kappa_a^*(\mu_{\nu_e})}\,. \tag{20}$$

In degenerate matter, as we shall show later in Sect. 3.1,

$$\kappa_a^*(\mu_{\nu_e}, T) \approx \frac{G_F^2}{2\pi}\,\frac{1+3g_A^2}{4}\,M^2T^2\mu_e \simeq \left(\frac{k_B T}{15\,\mathrm{MeV}}\right)^2\left(\frac{\mu_e}{200\,\mathrm{MeV}}\right)\,\frac{1}{20\,\mathrm{cm}} \tag{21}$$

where M is the nucleon mass, T is the temperature, and μ_e is the electron chemical potential. Using Eq. 20 and neglecting general relativistic corrections, we can approximate the lepton number flux in Eq. 9 as

$$F_L \approx \frac{n_b}{6\kappa_a^*} \frac{\partial Y_{\nu_e}}{\partial r} \,. \tag{22}$$

By noting that n_b/κ_a^* is a weak function of the density, we ignore its spatial dependence to find an analytic solution of the separable form $Y_\nu(r,t) = Y_{\nu,0}\phi(t)\psi(r)$ to Eq. 9, similar to the method described in Prakash et al. (1997). Using appropriate boundary conditions at the surface, we separately solve for spatial and temporal dependencies with $\phi(0) = 1$ and $\psi(0) = 1$. For the temporal part, which is of interest here, we obtain a simple exponential solution:

$$\phi(t) = \exp\left(\frac{-t}{\tau_D}\right) \quad \text{where} \quad \tau_D \simeq \frac{6\langle\kappa_a^*\rangle\, R^2}{C_x} \frac{\partial Y_L}{\partial Y_\nu} \,. \tag{23}$$

Here, $\langle\kappa_a^*\rangle$ represents a spatial average of the charged current opacity inside the PNS and the constant $C_x \simeq 10$ depends on $\psi(r)$. Using fiducial values $T = 15\,\mathrm{MeV}$ and $\mu_e = 200\,\mathrm{MeV}$ and $\partial Y_L/\partial Y_\nu = 5$ and setting $\langle\kappa_a^*\rangle = \kappa_a^*(\mu_e = 200\,\mathrm{MeV}, T = 15\,\mathrm{MeV})$, we obtain

$$\tau_D \approx 11 \left(\frac{R}{10\,\mathrm{km}}\right)^2 \left(\frac{k_B T}{15\,\mathrm{MeV}}\right)^2 \left(\frac{\mu_e}{200\,\mathrm{MeV}}\right) \left(\frac{\partial Y_L}{5\,\partial Y_\nu}\right) \quad s \,. \tag{24}$$

This result, albeit arrived at with some approximation, clearly reveals the microphysics. The dependence on T, μ_e, and $\partial Y_L/\partial Y_\nu$ is made explicit, and we discuss later in Sect. 3 how the dense matter EoS directly affects these properties.

We can also estimate the amount of Joule heating in the core: (see Eq. 19)

$$\dot{E}_{joule} = -n_b \mu_\nu \frac{\partial Y_L}{\partial t} \approx n_b \mu_\nu \frac{\partial Y_L}{\partial Y_\nu} \frac{Y_{\nu,0}}{\tau_D} \,, \tag{25}$$

where we have used Eq. 23 to express the result in terms of the deleptonization time. For typical values of the deleptonization time $\tau_D \sim 11$ s and $\partial Y_L/\partial Y_\nu \sim 5$, we find the heating rate per baryon $\dot{E}_{joule}/n_b \approx \mu_\nu Y_{\nu,0}/3$. At early times when $\mu_\nu \sim 150\,\mathrm{MeV}$ and $Y_{\nu,0} \sim 0.05$, the heating rate $\approx 2\,\mathrm{MeV}$ per baryon per second will result in a similar rate of change in the matter temperature. This, coupled with the positive temperature gradients, results in a net heating of the inner core when $t < \tau_D$.

After deleptonization when the core begins to cool, the second term in Eq. 19 can be neglected and the energy flux

$$H_\nu \approx \frac{T^3}{6\pi^2} D_4 \frac{\partial T}{\partial r} \,. \tag{26}$$

Energy transport is dominated by $\nu_\mu, \bar{\nu}_\mu, \nu_\tau, \bar{\nu}_\tau$, and $\bar{\nu}_e$ neutrinos since their charged-current reactions are suppressed and therefore they have larger mean free paths. For typical conditions where nucleons are degenerate and neutrino degeneracy is negligible, elastic neutral current scattering off nucleons is a dominant source of opacity and (see Sect. 3.1)

$$\kappa_s^*(E_\nu) \simeq \frac{5}{6\pi}\, G_F^2\, c_A^2\, \tilde{N}_0\, k_B T\, E_\nu^2\,, \tag{27}$$

where $\tilde{N}_0 = \sum_{i=n,p} \partial n_i/\partial \mu_i$ is the effective density of nucleon states at the Fermi surface to which neutrinos couple and $c_A \simeq 1.2$ is the axial vector coupling. Using Eq. 27 the diffusion coefficient D_4 in Eq. 26 can be written as

$$D_4 = \frac{\pi^3}{G_F^2 c_A^2\, \tilde{N}_0\, (k_B T)^3}\,. \tag{28}$$

Substituting Eq. 28 in Eq. 26, Eq. 19 can be solved with the separable ansatz $T(r,t) = T_c \psi(x)\phi(t)$ to find a self-similar solution. We find that the temporal part $\phi(t) = 1 - (t/\tau_c)$, where

$$\tau_c \approx \frac{2\pi G_F^2 c_A^2}{\beta} \left\langle N_0 \frac{3n_b}{\pi^2} \frac{\partial s}{\partial T} \right\rangle k_B T_c\, R^2 \simeq 10\, s\, \frac{k_B T_c}{30\,\mathrm{MeV}}\, \frac{\langle n_b^{2/3}\rangle}{n_0^{2/3}} \left(\frac{R}{12\,\mathrm{km}}\right)^2\,, \tag{29}$$

where $\langle\rangle$ denotes a spatial average, the numerical constant $\beta \cong 19$, and $n_0 = 0.16\,\mathrm{fm}^{-3}$. Additionally, we have used $\partial s/\partial T = \pi^2 N_0/3n_b$ and $N_0 = M(3\pi^2 n_b)^{1/3}/\pi^2$, which hold for a nonrelativistic, degenerate gas. The spatial averages and numerical value of β are obtained by solving for the function $\psi(r)$.

2.4 PNS Neutrino Emission

Here, we discuss the evolution of the flavor-dependent neutrino luminosities and average energies, which constitute the detectable signal from the PNS. We focus on the properties of the neutrinos near the surface of the PNS. As the neutrinos propagate through the rest of the star, neutrino oscillations can change the flavor content of the neutrino fields and alter the spectra of the neutrinos that eventually reach earth (Duan et al. 2010).

The evolution of the interior of the PNS drives the total energy and lepton number emitted from the surface, but the outermost layers of the PNS shape the spectrum of the emitted neutrinos. Therefore, it is convenient to describe the approximate

radius at which neutrinos that escape to infinity are emitted, the "neutrinosphere" R_ν. Following Keil et al. (2003) and Fischer et al. (2011), we define

$$\tau_{\rm therm}(R_\nu) = \int_{R_\nu}^{\infty} dr \sqrt{\langle\kappa_a\rangle(\langle\kappa_a\rangle + \langle\kappa_s\rangle)} = \frac{2}{3}, \tag{30}$$

where $\langle\kappa\rangle$ is an opacity averaged over the local neutrino distribution function. This is of course an approximation, since neutrino interactions have a strong energy dependence. Neutrinos of the same flavor but different energies will therefore decouple at different positions within the PNS. Nonetheless, the neutrino luminosity in a particular flavor can be reasonably estimated by assuming the neutrinosphere is a blackbody emitter

$$L_\nu = 4\pi\sigma_{BB}\phi R_\nu^2 T(R_\nu)^4, \tag{31}$$

where $\sigma_{BB} = 4.75 \times 10^{35}\,{\rm erg\,MeV^{-4}\,cm^{-2}\,s^{-1}}$ is the blackbody constant and ϕ is a factor of order unity that accounts for deviations from strict Fermi–Dirac blackbody emission (Hüdepohl et al. 2010; Mirizzi et al. 2015). For a pure blackbody spectrum, the average energy of the emitted neutrinos would be $\langle\varepsilon_\nu\rangle \approx 3.15T(R_\nu)$. The energy moments of neutrinos of species i at radius r are given by

$$\langle\varepsilon_{\nu_i}^n\rangle = \frac{\int_0^\infty d\varepsilon \int_{-1}^1 d\mu \varepsilon^{n+2} f_{\nu_i}}{\int_0^\infty d\varepsilon \int_{-1}^1 d\mu \varepsilon^2 f_{\nu_i}}. \tag{32}$$

In reality, high-energy neutrinos have a larger decoupling radius than lower-energy neutrinos due to the approximate ε_ν^2 scaling of the neutrino opacities (Keil et al. 2003). Therefore, high-energy neutrinos are emitted from regions with lower temperatures. The emitted neutrino spectra then have a "pinched" character, where there is a deficit of high-energy neutrinos relative to the Fermi–Dirac spectrum predicted by an energy-averaged neutrinosphere (Janka and Hillebrandt 1989).

The evolution of the neutrinosphere radii as a function of time is shown in the third panel, and the temperature at the neutrinospheres is shown in the fourth panel of Fig. 3. There are only small differences between the μ and τ flavored neutrino and antineutrino emission because they experience similar neutral current opacities. Therefore, we group all of these flavors together in flavor x. During the accretion phase and into the mantle contraction phase, there is a clear hierarchy with $R_{\nu_x} < R_{\bar{\nu}_e} < R_{\nu_e}$. This is driven mainly by differences in the charged-current opacities: electron neutrinos get a large opacity contribution from the reaction $\nu_e + n \rightarrow e^- + p$ due to the large number of neutrons present near the decoupling region, electron antineutrinos get a somewhat smaller contribution from $\bar{\nu}_e + p \rightarrow e^+ + n$ because of the small number of protons present in the decoupling region, and heavy flavored neutrinos receive no contribution to their opacity from charged current interactions. Since the temperature is decreasing with increasing

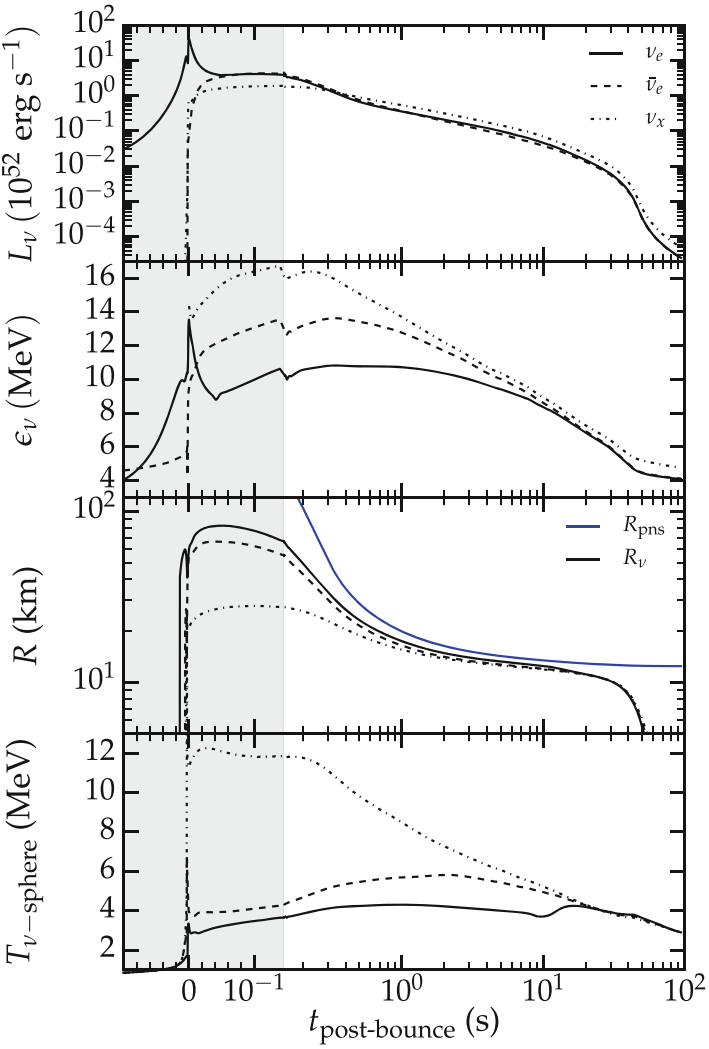

Fig. 3 Time evolution of neutrino properties at infinity and the properties of the neutrinospheres. The *gray region* corresponds to the accretion phase and is on a linear scale, while the region to the right is the PNS cooling phase and it is plotted on a logarithmic scale. We measure radiation quantities at a radius of 300 km or at the maximum radius of the simulation domain, whichever is smaller. At the transition from the accretion phase to the PNS cooling phase, all of the material from above the shock is excised from the grid, causing a slight jump in some quantities. In all of the panels, all heavy-flavor neutrinos are represented by ν_x, since their properties are all very similar. In the *top panel*, we show the neutrino luminosity for single flavors as a function of time. In the second panel, we show the evolution of the neutrino average energies. In the third panel, we show the evolution of the neutrinosphere radii, along with the PNS radius, as a function of time. The simulation covers the entire time the PNS is optically thick to neutrinos. The *bottom panel* shows the temperature at the neutrinospheres. Similar results can be found in Fischer et al. (2011)

radius, this gives rise to the standard early-time hierarchy of neutrino energies $\langle \varepsilon_{\nu_e} \rangle < \langle \varepsilon_{\bar{\nu}_e} \rangle < \langle \varepsilon_{\nu_x} \rangle$ during the accretion and mantle cooling phases that can be seen in the second panel of Fig. 3. During this period, inelastic scattering from electrons outside of the neutrinosphere reduces the average energies of heavy-flavor neutrinos relative to what the blackbody model would predict (Raffelt 2001). In the deleptonization phase, there are very few protons in the outer layers of the PNS. Therefore, the opacities for the electron antineutrinos and the heavy-flavor neutrinos are very similar and all of these neutrino flavors decouple at similar radii. In Fig. 3, these neutrinos have almost equal average energies over the majority of the PNS cooling phase. Eventually, during the thermal cooling phase, all the three neutrinospheres converge and the average emitted energies of all flavors become similar (Fischer et al. 2011), although the time at which they converge depends on how the charged-current opacities are calculated (Roberts et al. 2012).

The top panel of 3 shows the luminosities of individual flavors of neutrinos. Soon after shock breakout, the electron neutrino and antineutrino luminosities become very close to one another and stay similar throughout the entire cooling evolution. Deleptonization proceeds because the average energies of the electron neutrinos are lower, and more electron neutrinos are required to carry a fixed luminosity than electron antineutrinos. Due to their small neutrinosphere, the heavy-flavor neutrino luminosities are much lower than the electron neutrino luminosities during the mantle cooling phase. After mantle contraction, there is approximate equipartition of luminosity among the different flavors.

3 Physics that Shape the Cooling Signal

The PNS neutrino signal is interesting in part because it is shaped by the properties of neutron-rich material at densities and temperatures that are inaccessible in the laboratory. Because of the high densities encountered throughout the PNS, the internucleon separation is small enough that interactions between nuclei play a central role in determining the PNS EoS and the neutrino interaction rates. Over the past decade, improved models to describe hot and dense matter were developed that reproduce empirically known properties of symmetric nuclear matter at saturation density. However, since matter encountered in the proto-neutron stars is characterized by a small proton fraction $x_p \simeq 0.05 - 0.3$, the symmetry energy, defined through the relation

$$S(n_b) = E(n_b, x_p = 1/2) - E_n(n_b, x_p = 0)\,, \tag{33}$$

where $E(n_b, x_p = 1/2)$ is the energy per particle of symmetric nuclear matter and $E(n_b, x_p = 0)$ is the energy per particle of pure neutron matter, plays an important role. The energy of neutron-rich matter $E(n_b, x_p) \simeq E(n_b, x_p = 1/2) + S(n_b)(1 - 2x_p^2)$ since quartic and higher-order terms are found to be small in most theoretical calculations. In this context, ab initio calculations of the energy of neutron matter at subsaturation density (Gandolfi et al. 2011; Tews et al. 2013)

have provided valuable guidance in the development of a new suite of models for hot and dense matter which are also consistent with recent neutron star radii in the range 10–12 km. These smaller radii are favored by recent modeling efforts to extract the radius of neutron stars from X-ray observations of quiescent neutron star in low mass X-ray binaries and X-ray burst (Ozel et al. 2015; Steiner et al. 2013). The properties of matter at and around nuclear saturation density, especially $S(n_b)$, can influence deleptonization and neutrino cooling timescales, convection, and the neutrino spectrum (Roberts et al. 2012; Roberts et al. 2012; Sumiyoshi et al. 1995). PNS evolution is also sensitive to the thermal properties of degenerate dense matter as discussed in 2.3, and for a discussion of it, we refer the reader to Refs. Prakash et al. (1997), Constantinou et al. (2014), and Rrapaj et al. (2015). In the next two subsections, we describe how nuclear interactions can affect neutrino opacities and convective instabilities inside the PNS, both of which can alter the PNS cooling timescale.

At densities near and below nuclear saturation density, PNS matter is only composed of protons, neutrons, and electrons, but at higher densities, it is possible for more exotic material to be present. Hyperons–baryons containing strange quarks – can be produced in the interior of the PNS because the weak interaction does not conserve strangeness (Prakash et al. 1997). Quark matter (Pons et al. 2001b; Steiner et al. 2001) or Bose condensates (Pons et al. 2000, 2001a; Prakash et al. 1997) may also exist in the innermost regions of PNSs. In addition to altering the neutrino opacities, these new degrees of freedom serve to soften the nuclear EoS at high density and reduce the maximum neutron star mass. This can lead to "metastable" PNSs that emit neutrinos for tens of seconds before collapsing to a black hole (BH) when more exotic material forms in their core and pressure support is reduced. BH formation would abruptly end the neutrino signal and is therefore directly observable (Pons et al. 2001b). We do not discuss these effects in any more detail here, but refer the reader to Prakash et al. (1997).

3.1 Neutrino Opacities in Dense Matter

The neutrino scattering opacities and thereby the diffusion coefficients defined in Sect. 2.1 receive contributions from neutrino scattering, absorption, and pair production processes, as well as the inverses of the latter two. Scattering contributions come from the reactions

$$\begin{aligned} \nu_i + n &\rightleftharpoons \nu_i + n \\ \nu_i + p &\rightleftharpoons \nu_i + p \\ \nu_i + e^- &\rightleftharpoons \nu_i + e^- \\ \nu_i + e^+ &\rightleftharpoons \nu_i + e^+, \end{aligned}$$

as well as scattering from other possible components of the medium. All of the reactions above have neutral current contributions for all flavors of neutrinos,

while e^- and e^+ scattering also have a charged-current contribution for ν_e and $\bar{\nu}_e$ scattering, respectively. Since the dominant scattering contribution for all particles comes from the n and p scattering, there are only small differences between the scattering contributions to the diffusion coefficients for different neutrino flavors. Scattering from electrons and positrons can be highly inelastic, due to the small mass of the electron relative to the characteristic PNS neutrino energy, while scattering from neutrons and protons is close to elastic. This inelasticity can alter the emitted neutrino spectrum and serves to bring the average energies of the different neutrino species closer to one another (Hüdepohl et al. 2010).

The diffusion coefficients for the various neutrino flavors become different from one another due to charged-current neutrino interactions. The main absorption contribution to $D_i^{\nu_e}$ comes from

$$e^- + p \rightleftharpoons \nu_e + n,$$

while the main absorption contribution to $D_i^{\bar{\nu}_e}$ comes from

$$e^+ + n \rightleftharpoons \bar{\nu}_e + p.$$

All of the opacities receive contributions from thermal processes such as

$$N + N \rightarrow N + N + \nu + \bar{\nu}$$
$$e^- + e^+ \rightarrow \nu + \bar{\nu},$$

but these are usually small compared to the charged-current interactions that affect the electron neutrinos and antineutrinos.

For both scattering and absorption processes, the cross section per unit volume for a general process $\nu + 2 \rightarrow 3 + 4$ (where particle 3 is either a neutrino, electron, or positron) can be written as (Reddy et al. 1998)

$$\kappa(\varepsilon_\nu) = \frac{2}{2\varepsilon_\nu (2\pi)^9} \int \frac{d^3p_2}{2\varepsilon_2} \int \frac{d^3p_3}{2\varepsilon_3} \int \frac{d^3p_4}{2\varepsilon_4} f_2(\varepsilon_2)(1 - f_3(\varepsilon_3))(1 - f_4(\varepsilon_4)) \times (2\pi)^4 \delta^4 (P_\nu + P_2 - P_3 - P_4) \langle |\mathscr{M}|^2 \rangle, \tag{34}$$

where

$$\langle |\mathscr{M}|^2 \rangle = 16 G_F^2 \left[(C_V^2 + C_A)^2 (P_\nu \cdot P_2)(P_3 \cdot P_4) + (C_V - C_A)^2 (P_2 \cdot P_3)(P_\nu \cdot P_4) - (C_V^2 - C_A^2) M_2 M_4 (P_\nu \cdot P_3) \right] \tag{35}$$

is the spin-summed weak interaction matrix element of the process, C_V and C_A are the vector and axial coupling constants, δ^4 is the four-dimensional Dirac delta function, $P_i = (\varepsilon_i, -\mathbf{p}_i)$ is the relativistic four-momentum, p_i is the three-momentum, ε_i is the energy, and f_i is the distribution of species i. Particles 2 and

4 are always in thermal equilibrium inside PNSs, so f_2 and f_4 are isotropic Fermi–Dirac distribution functions. This expression comes directly from Fermi's golden rule. If we specialize to particles 2 and 4 being nucleons, the reduced matrix element becomes independent of the nucleon momenta at leading order v/c, and the cross section can be written as

$$\kappa(\varepsilon_\nu) = \frac{G_F^2}{(2\pi)^2} \int_{-1}^{1} d\mu_3 (C_V^2(1+\mu_3) + C_A^2(3-\mu_3)) \int_0^\infty d\varepsilon_3 p_3 \varepsilon_3 (1 - f_3(\varepsilon_3)) S(q_0, q), \tag{36}$$

where C_V and C_A are weak vector and axial–vector coupling constants of the weak interaction, $\mu_3 = \mathbf{p_\nu} \cdot \mathbf{p_3}/(|\mathbf{p_\nu}||\mathbf{p_3}|)$, and

$$S(q_0, q) = 2 \int \frac{d^3 p_2}{(2\pi)^3} \int \frac{d^3 p_4}{(2\pi)^3} f_2(\varepsilon_2)(1 - f_4(\varepsilon_4))(2\pi)^4 \delta^4 (Q + P_2 - P_4) \tag{37}$$

The energy–momentum transfer from the neutrino to the nucleons is denoted by the four-vector $Q = (q_0, -\mathbf{q})$, such that $\varepsilon_3 = \varepsilon_\nu - q_0$ and $q = |\mathbf{q}| = \sqrt{\varepsilon_\nu^2 + \varepsilon_3^2 - 2\varepsilon_\nu \varepsilon_3 \mu_3}$. This form of the opacity separates the contribution of the nucleons (or the "medium") from the neutrino and the outgoing particle (be it another particle or a neutrino with a different energy). The function $S(q_0, q)$ is often referred to as the response function or structure factor. A similar separation is found when the full-momentum dependence of the matrix element is included, although there are multiple response functions with different kinematic dependence (Reddy et al. 1998). The contribution to the cross section from particle 3 is the amount of phase space available to it in the final state, which results in the leading order ε_ν^2 dependence of weak interaction cross sections when $q_0 \sim 0$.

The response function includes the effects of energy/momentum conservation, Pauli blocking of the final-state nucleons, and thermal motion of the nucleons. When the momentum transfer q is small (so that $\mathbf{p}_2 = \mathbf{p}_4$), the response simplifies significantly. After manipulating the Fermi–Dirac distribution functions and integrating, one finds

$$S(q_0, 0) = 2\pi \delta(q_0) \frac{n_2 - n_4}{1 - \exp((\mu_4 - \mu_2)/T)}. \tag{38}$$

When species 2 and 4 are nondegenerate, this reduces to $2\pi\delta(q_0) n_2$. This response is purely elastic, since $q_0 = 0$ and $\varepsilon_\nu = \varepsilon_3$. For scattering reactions, when species 2 equals species 4, this response becomes

$$S_{\mathrm{scat}}(q_0, 0) = 2\pi \delta(q_0) T \frac{\partial n_2}{\partial \mu_2}. \tag{39}$$

In the degenerate limit, the response can be shown to be (Reddy et al. 1998)

$$S_{\rm deg}(q_0, q) = \frac{M^2(q_0 + \mu_2 - \mu_4)}{\pi q} \frac{\Theta(q - p_{F_2} + p_{F_4})}{1 - \exp((\mu_4 - \mu_2 - q_0)/T)}, \tag{40}$$

where p_{F_i} is the Fermi momentum of particles of species i and Θ is the Heaviside step function. The opacity then becomes

$$\kappa(\varepsilon_\nu) = \frac{G_F^2}{4\pi^3}(C_V^2 + 3C_A^2)M^2T^2(\varepsilon_\nu + \mu_2 - \mu_4)\Xi \frac{\pi^2 + \left(\frac{\varepsilon_\nu - \mu_\nu}{T}\right)^2}{1 + \exp((\mu_\nu - \varepsilon_\nu)/T)}, \tag{41}$$

where

$$\Xi = \Theta(p_{F_4} + p_{F_3} - p_{F_2} - p_{F_\nu}) + \frac{p_{F_4} + p_{F_3} - p_{F_2} + p_{F_\nu}}{2\varepsilon_\nu}\Theta(p_{F_\nu} - |p_{F_4} + p_{F_3} - p_{F_2}|). \tag{42}$$

When neutrinos are degenerate, only neutrinos near the Fermi surface will be able to scatter. The relevant opacity is then

$$\kappa(\mu_\nu) = \frac{G_F^2}{8\pi}(C_V^2 + 3C_A^2)M^2(k_BT)^2\mu_3, \tag{43}$$

where we have assumed all four species are in equilibrium, $\mu_\nu + \mu_2 = \mu_3 + \mu_4$. These results are used in Sect. 2.3 to estimate the deleptonization and thermal cooling timescales.

If nucleon–nucleon interactions are also considered, they can alter the response of the medium in a number of ways (Burrows and Sawyer 1998; Hannestad and Raffelt 1998; Horowitz and Pérez-García 2003; Reddy et al. 1998, 1999). The simplest way to include nucleon–nucleon interactions is in the mean field approximation. In this approximation, the average interaction with all other nucleons gives single nucleons a momentum-independent potential energy and an effective in-medium mass. The nucleon energy–momentum relation then becomes $\varepsilon_{2,4} = p_{2,4}^2/2m_{2,4}^* + U_{2,4}$. In the zero momentum transfer limit, the response becomes (Reddy et al. 1998)

$$S_{\rm MF}(q_0, 0) = 2\pi\delta(q_0 + \Delta U)\frac{n_2 - n_4}{1 - \exp((\mu_4 - \mu_2 + \Delta U)/T)}, \tag{44}$$

where $\Delta U = U_2 - U_4$. This implies that $\varepsilon_3 = \varepsilon_\nu + \Delta U$. Because the cross section strongly depends on the phase space available to particle 3, a large, positive ΔU can increase the neutrino cross section, while a negative ΔU will reduce the cross section (Martínez-Pinedo et al. 2012; Roberts et al. 2012). The potential energy of

neutrons, U_n, differs from the potential energy of protons, U_p, due to the isospin dependence of the nuclear interaction. In neutron-rich material, neutrons have a larger potential energy than protons because of the large, positive nuclear symmetry energy, $S(n_b)$, throughout the PNS. In fact, the potential energy difference can be related directly to the nuclear symmetry energy (Hempel 2015). Therefore, mean field corrections to the response in PNSs increase the cross section for $\nu_e + n \rightarrow e^- + p$ and decrease the cross section for $\bar{\nu}_e + p \rightarrow e^+ + n$. This change alters D_2 and D_3 and thereby the PNS deleptonization rate (Roberts 2012). These corrections can also move the electron neutrinosphere to a larger radius and the electron antineutrinosphere to a smaller radius. This increases the difference between $\langle \varepsilon_{\nu_e} \rangle$ and $\langle \varepsilon_{\bar{\nu}_e} \rangle$, which may have large consequences for nucleosynthesis near the PNS (see Sect. 4.3) (Martínez-Pinedo et al. 2012; Roberts 2012).

When the neutrino wavelength is long compared to the internucleon separation distance, neutrino interactions with the medium concurrently involve multiple nucleons at a microscopic level. In this limit, collective properties induced by nuclear interactions can significantly alter the response of the nuclear medium. The mean field approximation does not account for possible nucleon–nucleon correlations induced by interactions. Generally, accounting for these correlations is a complex many-body problem which has only been tackled within the random-phase approximation (RPA) (Burrows and Sawyer 1998; Reddy et al. 1999). The RPA essentially accounts for weak charge screening, which can reduce the neutrino opacity. In Fig. 4, we show the suppression of the diffusion coefficients by correlations. At high density, the corrections can be larger than a factor of two. This serves to decrease the cooling timescale of the PNS (Burrows and Sawyer 1998; Hüdepohl et al. 2010; Reddy et al. 1999; Roberts et al. 2012). In Fig. 5, we show models of PNS cooling that include RPA corrections to the neutrino

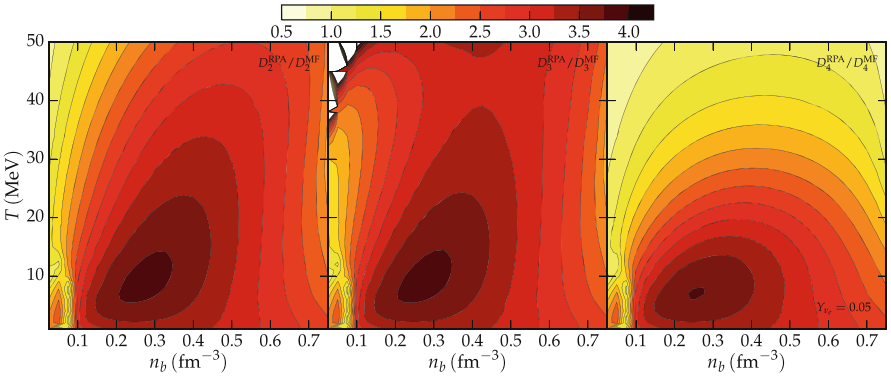

Fig. 4 Ratio of diffusion coefficients not including nuclear correlations to diffusion coefficients including nuclear correlations. At high density, weak charge screening (calculated using the random-phase approximation) suppresses the neutrino opacity and increases the neutrino diffusion coefficients. This reduces the PNS cooling timescale

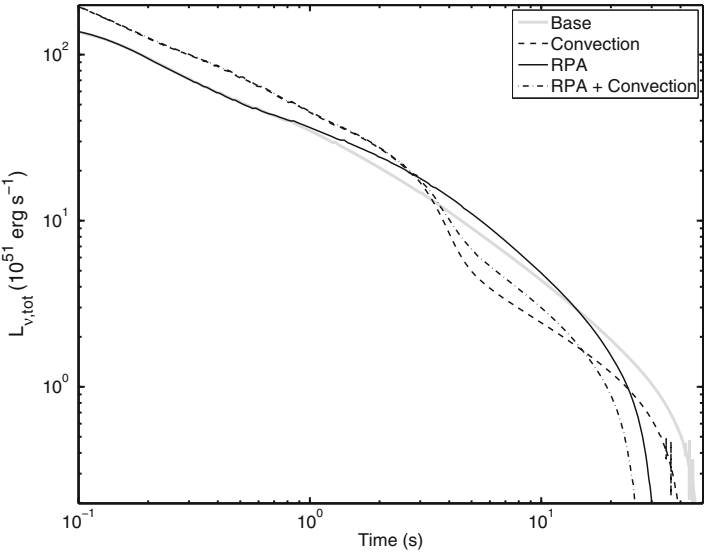

Fig. 5 The total PNS neutrino luminosity versus time for a number of PNS models that include convection and/or the effect of nuclear correlations on the opacity. Both convection and nuclear correlations decrease the cooling timescale relative to the baseline model. Convection alters the luminosity at early times, while correlations only become important after the mantle cooling phase. The models shown here are similar to those described in Roberts et al. (2012)

interaction rates compared with those that do not. During the mantle contraction phase, they have little effect because the neutrino luminosity originates in a low-density region. Once the neutrino luminosity is determined at higher densities, during the deleptonization and thermal cooling phases, these corrections decrease the neutrino emission timescale. The magnitude of this effect depends on the assumed nucleon–nucleon interaction (Keil et al. 1995; Reddy et al. 1999; Roberts et al. 2012).

3.2 PNS Convection

In addition to neutrinos, hydrodynamic motions of the PNS can transport energy and lepton number through the star. Although the majority of the PNS is in hydrostatic equilibrium, there can be regions which are unstable to the development of convection. Similar to the case in normal stellar burning, convective overturn can transport energy and lepton number much more rapidly than radiation and shorten the cooling timescale (Burrows 1987; Roberts et al. 2012; Wilson and Mayle 1988).

The standard Ledoux criterion for convective instability, adapted to the conditions found inside a PNS, is given by

$$\omega_C^2 = -\frac{g}{\gamma_{n_b}} \left(\gamma_s \nabla \ln(s) + \gamma_{Y_L} \nabla \ln(Y_L)\right) > 0, \tag{45}$$

where g is the local acceleration due to gravity and

$$\gamma_{n_b} = \left(\frac{\partial \ln P}{\partial \ln n_b}\right)_{s,Y_L}, \gamma_s = \left(\frac{\partial \ln P}{\partial \ln s}\right)_{n_b,Y_L}, \gamma_{Y_L} = \left(\frac{\partial \ln P}{\partial \ln Y_L}\right)_{n_b,s}.$$

These last three quantities are only functions of the nuclear EoS. In particular, γ_{n_b} is related to the sound speed and γ_{n_b} and γ_s are always positive. The third thermodynamic derivative, γ_{Y_L}, can either be positive or negative; the pressure receives contributions from both electrons which have $\partial P_e/\partial Y_e > 0$ and from the nucleons for which $\partial P_N/\partial Y_e < 0$ when $Y_e < 0.5$ due to variations in $\partial S(n_b)/\partial n_b$ where $S(n_b)$ is the nuclear symmetry energy defined in Eq. 33 (Roberts et al. 2012). Noting that $\partial Y_e/\partial Y_L > 0$ and of order unity, it is easy to see that the sign of γ_{Y_L} can change depending on the relative contributions of electrons and nucleons. Therefore, the portion of the PNS that is convectively unstable depends on the assumed nuclear EoS and its symmetry energy, as well as the gradients of entropy and Y_L (Roberts et al. 2012). The PNS may also be subject to double-diffusive instabilities due to the lateral transport of composition and energy by neutrinos (Wilson and Mayle 1988). These double-diffusive instabilities would extend the region over which the PNS was unstable to hydrodynamic overturn.

The outer PNS mantle is unstable to adiabatic convection soon after the passage of the bounce shock (Epstein 1979). This early period of instability beneath the neutrinospheres has been studied extensively in both one and two dimensions with the hope that it could increase the neutrino luminosities enough to lead to a successful CCSN explosion (Buras et al. 2006; Wilson and Mayle 1988). During the deleptonization and thermal cooling phases, more and more of the PNS becomes unstable to convection because of the entropy and lepton gradients produced by neutrino cooling. Figure 1 shows that there are negative entropy gradients throughout the mantle for the entirety of the PNS phase, and the negative gradient extends through the whole PNS by the end of deleptonization.

Because the cooling timescale is much longer than the dynamical timescale of the PNS, multidimensional simulations of late-time PNS convection have not been carried out to date. Rather, mixing length theory has been employed to study the impact of convection on the late-time neutrino signal (Burrows 1987; Mirizzi et al. 2015; Roberts et al. 2012). In Fig. 5, we show the total neutrino luminosity for models with and without convection to highlight the impact convection can have on the cooling timescale. At early times, the luminosity is elevated by around 25 % due to convection until the period of convective instability ceases a few seconds after bounce. After this the luminosity is depressed relative to the case without convection, and the overall cooling timescale is reduced.

4 Observable Consequences

4.1 Neutrinos from SN 1987A

Up to now, our discussion of PNS cooling has been mostly theoretical. In fact, the basic features of PNS cooling were reasonably well characterized before there was any observational evidence for this picture (Burrows and Lattimer 1986). In February of 1987, both photons (Kunkel et al. 1987) and neutrinos (Alexeyev et al. 1988; Bionta et al. 1987; Hirata et al. 1987) reached Earth from a massive star that collapsed in the Large Magellanic Cloud, SN 1987A. Of course, the neutrinos are of the most interest for constraining PNS evolution, since the optical depth near the PNS is far too high for photons to escape this region. Bursts of sixteen, eight, and five neutrinos were observed near the time of SN 1987A in the Kamiokande (Hirata et al. 1987), IMB (Bionta et al. 1987), and Baksan (Alexeyev et al. 1988) neutrino detectors, respectively. Although there were only ∼30 electron antineutrino events detected, they provided general confirmation of the previously developed theoretical picture of neutrino emission during core collapse and subsequent PNS cooling (Burrows and Lattimer 1987). The neutrinos were observed within a 23-second window at Kamiokande and had energies ranging between 5 and 30 MeV. It is worth mentioning that this implies a PNS survived in the core of SN 1987A for at least 20 s, even though no central object has been observed in the remnant of SN 1987A to date (Graves et al. 2005).

In Fig. 6, the joint probability distribution of the electron antineutrino spectral temperature and PNS cooling timescale inferred from the detected SN 1987A neutrino events by Loredo and Lamb (2002). They model the PNS cooling phase with a luminosity falling off with time as $L_{\bar{\nu}_e}(t) \propto (1 + t/\tau_c)^{-4}$ and Fermi–Dirac neutrino spectrum with temperature $T_{\bar{\nu}_e} = T_{c,0}(1 + t/\tau_c)^{-1}$. The neutrino cooling timescale is best fit with $\tau_c = 14.7$ s, and the antineutrino average energy at 1 s after bounce is best fit by $\langle \varepsilon_{\bar{\nu}_e} = 13.7$ MeV. This is in reasonable qualitative agreement with the models in the literature and the one presented in Sect. 2.4. It is quite an achievement that models of PNS cooling based on theoretical considerations alone before 1987 were able to reproduce the general features of the SN 1987A neutrino signal. Nevertheless, there is uncertainty in the cooling timescale and $T_{c,0}$. Additionally, attempts have been made to constrain various physical processes operating during PNS cooling using the SN 1987A neutrino data (Burrows and Lattimer 1987; Keil et al. 1995; Reddy et al. 1999).

The neutrino cooling signal from SN 1987A has also been used to constrain beyond the standard model physics. Essentially, it is possible for exotic particles with very weak – but not too weak – interactions to rapidly remove energy from the PNS (Raffelt 1996). If the amount of energy removed is comparable to the amount of energy emitted in neutrinos, the neutrino cooling timescale can be shortened. This technique has been mainly used to put limits on the properties of axions using the SN 1987A neutrino signal (Keil et al. 1997).

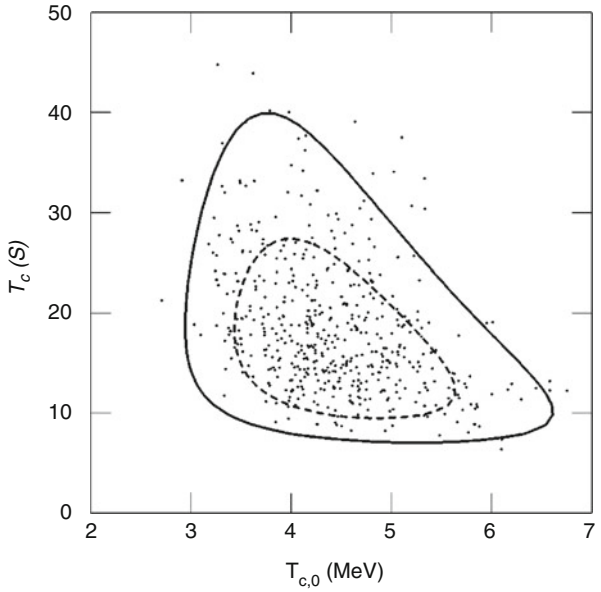

Fig. 6 Probability contours of the PNS cooling timescale, τ_c, and the antielectron neutrino spectral temperature $T_{c,0}$ based on the SN 1987A neutrinos observed at the Super-Kamiokande, Baksan, and IMB detectors (Taken from Loredo and Lamb (2002)). The *dashed* and *solid lines* demarcate regions of 68 % and 95 % credibility for the PNS cooling parameters, respectively. These inferred parameters are in good qualitative agreement with the predictions from models of PNS cooling. In this model, the average electron antineutrino energy is given by $\langle \varepsilon_{\bar{\nu}_e} \rangle \approx 3.15 T_{\bar{\nu}_e} \approx 13.7\,\mathrm{MeV}$, where the last value is the value at 1 s post-bounce (Reprinted figure with permission from Loredo and Lamb (2002). Copyright 2002 by the American Physical Society)

4.2 Galactic Supernova Neutrinos

Any future galactic SN will yield far more neutrino detections than SN 1987A. The expected rate of CCSN in the Milky Way is around 1–2 per century (Cappellaro and Turatto 2001), so direct CCSN detection is somewhat of a waiting game. Because of this, there are no dedicated CCSN neutrino detectors, but luckily there are many neutrino experiments that can moonlight as CCSN neutrino observatories.

The neutrino detection rate for a galactic CCSN can be found by integrating the neutrino distribution function at Earth over the response of the neutrino detector (Pons et al. 1999; Scholberg 2012):

$$\frac{dN}{dt} = \frac{2\pi n_d}{(2\pi)^3} \int_0^\infty d\varepsilon_\nu \varepsilon_\nu^2 \sigma_\nu(\varepsilon_\nu) W(\varepsilon_\nu) \int_{-1}^{1} d\mu\, f_\nu(\varepsilon_\nu, \mu, D)$$
$$\approx 87.5\,\mathrm{s}^{-1} \left(\frac{D}{10\,\mathrm{kpc}}\right)^{-2} \left(\frac{\mathscr{M}_{\mathrm{det}}}{32\,\mathrm{kt}}\right) \left(\frac{L_{\bar{\nu}_e}}{10^{51}\,\mathrm{erg\,s}^{-1}}\right) \left(\frac{\langle \varepsilon_{\bar{\nu}_e} \rangle}{12\,\mathrm{MeV}}\right) G[f_{\bar{\nu}_e}(\varepsilon)], \tag{46}$$

where D is the distance from Earth to the SN, n_d is the number of particles available to interact with neutrinos in the detector, and $W(\varepsilon)$ is the detector efficiency as a function of energy. In the second line, we estimate the electron antineutrino detection rate in a Cherenkov water detector with detector mass $\mathscr{M}$. The detector parameters chosen are meant to approximately correspond to the properties of Super-Kamiokande (Fukuda et al. 2003). The dimensionless factor

$$G[f_\nu(\varepsilon)] = \frac{m_e^2 \int_0^\infty d\varepsilon \varepsilon^2 \sigma_\nu(\varepsilon) W(\varepsilon) f_\nu}{\sigma_\nu(\varepsilon = m_e)\langle \varepsilon_\nu \rangle^2 \int_0^\infty d\varepsilon \varepsilon^2 f_\nu} \tag{47}$$

encodes the spectral distribution of the neutrinos folded with the neutrino cross section and detector response. The presence of a detector threshold in $W(\varepsilon)$ can make the dependence of the count rate on the neutrino average energy steeper than is suggested by the simple scaling relation above. For a Fermi–Dirac distribution of neutrinos with zero chemical potential, W has a value ≈ 1.8. Integrating over a predicted CCSN neutrino signal, Scholberg (2012) find that around 7,000 electron antineutrino events would be detected in Super-Kamiokande for a SN 10 kpc away and that the majority of these neutrinos would come from the PNS cooling phase (Mirizzi et al. 2015). Additionally, electron neutrinos will be detectable in liquid argon detectors through the reaction $\nu_e + {}^{40}Ar \rightarrow e^- + {}^{40}K$. For a supernova at 10 kpc, we can expect about 700 events per kiloton (Scholberg 2012). The $\simeq$40 kiloton liquid argon detector planned at the Deep Underground Neutrino Experiment (DUNE) will be able to provide valuable and complementary information about flavor and lepton number when combined with water Cherenkov detectors. Together, the large number of events and high-energy resolution available from the current suite of neutrino experiments will put much more stringent constraints on the interior properties of PNSs when the next galactic CCSN is detected.

It is also possible that current neutrino detectors with upgrades or next-generation neutrino detectors will be able to observe the diffuse background of neutrinos produced by CCSNe over the lifetime of the universe (Horiuchi et al. 2009). Predictions for the diffuse MeV scale neutrino background density depend on the integrated spectrum of neutrinos emitted during CCSNe, especially during the PNS cooling phase (Nakazato et al. 2015).

4.3 Impact on CCSN Nucleosynthesis

Neutrinos can alter the composition of material that is ejected from CCSNe, mainly in the innermost ejected regions (Woosley et al. 2002). The ejecta most affected by neutrinos are the material that comes from the surface of the PNS. Neutrino energy deposition in the atmosphere of the PNS can provide enough energy to unbind material from the surface and produce a neutrino-driven wind (Duncan et al. 1986). Once the outflowing material reaches large radii, the temperature drops and heavy nuclei form in the wind. The heating is driven by the charged-current reactions

$$\nu_e + n \rightarrow e^- + p \text{ and}$$
$$\bar{\nu}_e + p \rightarrow e^+ + n.$$

So, in addition to energizing the ejected material, neutrino interactions change its composition. The gravitational binding energy of a baryon at the surface of the PNS is $GM_{\rm pns}m_N/r_{\rm pns} \approx 160\,{\rm MeV}$, so a baryon must undergo between ten and fifteen neutrino captures (given the expected average neutrino energies discussed above) to escape the potential well of the PNS. This number of interactions is large enough to push the material to a composition where electron neutrino capture balances electron antineutrino capture, which results in an electron fraction (Qian and Woosley 1996)

$$Y_{e,\rm NDW} = \frac{\lambda_{\nu_e}}{\lambda_{\nu_e} + \lambda_{\bar{\nu}_e}}. \tag{48}$$

The neutrino capture rates are proportional to $\lambda_{\nu_e} \propto \dot{N}_{\nu_e}\langle(\varepsilon_{\nu_e} + \Delta_{np})^2\rangle/r^2$ and $\lambda_{\bar{\nu}_e} \propto \dot{N}_{\bar{\nu}_e} F^N_{\bar{\nu}_e}\langle(\varepsilon_{\nu_e} - \Delta_{np})^2\rangle/r^2$, where $\Delta_{np} = 1.293\,{\rm MeV}$ is the neutron–proton rest mass difference. Which heavy nuclei form depends very strongly on the electron fraction – as well as the entropy and dynamical timescale – of the outflowing material (Arcones and Thielemann 2013; Fischer et al. 2010; Hüdepohl et al. 2010; Nakazato et al. 2013; Roberts et al. 2012; Sumiyoshi et al. 1995; Woosley et al. 1994). Therefore, the final composition depends on the difference between the average energies of electron neutrinos and antineutrinos. The magnitude of this difference in numerical models of PNS cooling is sensitive to the mean field corrections discussed in Sect. 3.1, as well as to the method of neutrino transport (Fischer et al. 2010; Hüdepohl et al. 2010). It seems that the wind is at most marginally neutron rich, but this result depends on the properties of the assumed nuclear EoS (Hempel 2015; Mirizzi et al. 2015; Roberts et al. 2012).

The ν-process is another mechanism by which PNS neutrinos can alter the composition of the material ejected from CCSNe (Woosley et al. 1990). Here, unlike in the neutrino-driven wind, both charged-current and neutral current neutrino interactions are responsible for altering the composition of the material. Therefore, neutrinos of all flavors contribute to the process. Essentially, the ν-process alters the composition of ejected stellar material by the reactions

$$\begin{aligned}(Z,N) + \nu \rightarrow (Z,N)^* + \nu' &\rightarrow (Z,N-1) + n + \nu' \\ &\rightarrow (Z-1,N) + p + \nu' \\ &\rightarrow (Z-2,N-2) + \alpha + \nu', \\ (Z,N) + \nu_e &\rightarrow (Z+1,N-1) + e^-, \text{ and} \\ (Z,N) + \bar{\nu}_e &\rightarrow (Z-1,N+1) + e^+, \end{aligned} \tag{49}$$

where (Z,N) denotes a nucleus containing Z protons and N neutrons and $(Z,N)^*$ denotes an excited state of that nucleus. This is likely responsible for the production

rare isotopes, such as ^{11}B, ^{19}F, ^{15}N ^{138}La, and ^{180}Ta, from much more common nuclei in the envelope of the SN. Additionally, it has been suggested that neutrons produced by neutrino interactions in the helium shell can be rapidly captured on preexisting heavy nuclei and make the r-process (Epstein et al. 1988), although later work has shown it is challenging to achieve the requisite conditions for this process (Banerjee et al. 2011). The nuclear yields produced by this process are sensitive to the time-integrated flux and spectrum of neutrino incident on the exterior material (Heger et al. 2005). Therefore, the properties of PNS neutrino emission, along with neutrino oscillations above the PNS, are very important to determine the results of ν-process nucleosynthesis (Banerjee et al. 2011; Heger et al. 2005).

For further details on the impact of neutrinos on CCSNe nucleosynthesis, see the chapters "Effect of neutrinos on the ejecta composition of core collapse supernovae" and "Production of r-process elements in core collapse supernovae."

5 Cross-References

- Diffuse Neutrino Flux from Supernovae
- Making the Heaviest Elements in a Rare Class of Supernovae
- Neutrinos and Their Impact on Core-Collapse Supernova Nucleosynthesis
- Neutrino Emission from Supernovae

Acknowledgements We acknowledge our collaborators on this subject, including Gang Shen, Vincenzo Cirigliano, Jose Pons, Stan Woosley, and Ermal Rrapaj. LR was supported by NASA through an Einstein Postdoctoral Fellowship grant numbered PF3-140114 awarded by the Chandra X-ray Center, which is operated by the Smithsonian Astrophysical Observatory for NASA under contract NAS8-03060.

References

Alexeyev EN, Alexeyeva LN, Krivosheina IV, Volchenko VI (1988) Detection of the neutrino signal from SN 1987A in the LMC using the INR Baksan underground scintillation telescope. Phys Lett B 205:209–214. doi:10.1016/0370-2693(88)91651-6

Arcones A, Thielemann FK (2013) Neutrino-driven wind simulations and nucleosynthesis of heavy elements. J Phys G Nucl Phys 40(1):013201. doi:10.1088/0954-3899/40/1/013201. 1207.2527

Baade W, Zwicky F (1934) On super-novae. Proc Natl Acad Sci 20:254–259. doi:10.1073/pnas.20.5.254

Banerjee P, Haxton WC, Qian YZ (2011) Long, cold, early r-process? Neutrino-induced nucleosynthesis in He shells revisited. Phys Rev Lett 106(20):201104. doi:10.1103/PhysRevLett.106.201104. 1103.1193

Bionta RM, Blewitt G, Bratton CB, Casper D, Ciocio A, Claus R et al (1987) Observation of a neutrino burst in coincidence with supernova 1987A in the large magellanic cloud. Physi Rev Lett 58:1494–1496. doi:10.1103/PhysRevLett.58.1494

Buras R, Rampp M, Janka H, Kifonidis K (2006) Two-dimensional hydrodynamic core-collapse supernova simulations with spectral neutrino transport. I. Numerical method and results for a 15 Mȯ star. Astron Astrophys 447:1049–1092. doi:10.1051/0004-6361:20053783. arXiv:astro-ph/0507135

Burrows A (1987) Convection and the mechanism of type II supernovae. Astrophys J Lett 318:L57–L61. doi:10.1086/184937
Burrows A, Lattimer JM (1986) The birth of neutron stars. Astrophys J 307:178–196. doi:10.1086/164405
Burrows A, Lattimer JM (1987) Neutrinos from SN 1987A. Astrophys J Lett 318:L63–L68. doi:10.1086/184938
Burrows A, Sawyer RF (1998) Effects of correlations on neutrino opacities in nuclear matter. Phys Rev C 58:554–571. doi:10.1103/PhysRevC.58.554. arXiv:astro-ph/9801082
Burrows A, Reddy S, Thompson TA (2006) Neutrino opacities in nuclear matter. Nucl Phys A 777:356–394. doi:10.1016/j.nuclphysa.2004.06.012. arXiv:astro-ph/0404432
Cappellaro E, Turatto M (2001) Supernova types and rates. In: Vanbeveren D (ed) The influence of binaries on stellar population studies, astrophysics and space science library, vol 264, p 199. doi:10.1007/978-94-015-9723-4_16. astro-ph/0012455
Constantinou C, Muccioli B, Prakash M, Lattimer JM (2014) Thermal properties of supernova matter: the bulk homogeneous phase. Phys Rev C89(6):065,802. doi:10.1103/PhysRevC.89.065802. 1402.6348
Duan H, Fuller GM, Carlson J, Qian YZ (2006) Simulation of coherent nonlinear neutrino flavor transformation in the supernova environment: correlated neutrino trajectories. Phys Rev D 74(10):105014. doi:10.1103/PhysRevD.74.105014. arXiv:astro-ph/0606616
Duan H, Fuller GM, Qian YZ (2010) Collective neutrino oscillations. Ann Rev Nucl Part Sci 60:569–594. doi:10.1146/annurev.nucl.012809.104524. 1001.2799
Duncan RC, Shapiro SL, Wasserman I (1986) Neutrino-driven winds from young, hot neutron stars. Astrophys J 309:141–160. doi:10.1086/164587
Epstein RI (1979) Lepton-driven convection in supernovae. Mon Not R Astro Soc 188:305–325
Epstein RI, Colgate SA, Haxton WC (1988) Neutrino-induced r-process nucleosynthesis. Phys Rev Lett 61:2038–2041. doi:10.1103/PhysRevLett.61.2038
Fischer T, Martínez-Pinedo G, Hempel M, Liebendörfer M (2011) Neutrino spectra evolution during proto-neutron star deleptonization. ArXiv e-prints 1112.3842
Fischer T, Whitehouse SC, Mezzacappa A, Thielemann FK, Liebendoerfer M (2010) Protoneutron star evolution and the neutrino-driven wind in general relativistic neutrino radiation hydrodynamics simulations. Astron Astrophys 517:A80+. doi:10.1051/0004-6361/200913106
Fukuda S, Fukuda Y, Hayakawa T, Ichihara E, Ishitsuka M, Itow Y et al (2003) The super-kamiokande detector. Nucl Instrum Methods A 501:418–462. doi:10.1016/S0168-9002(03)00425-X
Gandolfi S, Carlson J, Reddy S (2011) The maximum mass and radius of neutron stars and the nuclear symmetry energy. ArXiv e-prints 1101.1921
Graves GJM, Challis PM, Chevalier RA, Crotts A, Filippenko AV, Fransson C, Garnavich P, Kirshner RP, Li W, Lundqvist P, McCray R, Panagia N, Phillips MM, Pun CJS, Schmidt BP, Sonneborn G, Suntzeff NB, Wang L, Wheeler JC (2005) Limits from the hubble space telescope on a point source in SN 1987A. Astrophys J 629:944–959. doi:10.1086/431422. astro-ph/0505066
Hannestad S, Raffelt G (1998) Supernova neutrino opacity from nucleon-nucleon bremsstrahlung and related processes. Astrophys J 507:339–352. doi:10.1086/306303. arXiv:astro-ph/9711132
Heger A, Kolbe E, Haxton WC, Langanke K, Martínez-Pinedo G, Woosley SE (2005) Neutrino nucleosynthesis. Phys Lett B 606:258–264. doi:10.1016/j.physletb.2004.12.017. arXiv:astro-ph/0307546
Hempel M (2015) Nucleon self-energies for supernova equations of state. Phys Rev C 91(5):055807. doi:10.1103/PhysRevC.91.055807. 1410.6337
Hirata K, Kajita T, Koshiba M, Nakahata M, Oyama Y, Sato N et al (1987) Observation of a neutrino burst from the supernova SN 1987A. Phys Rev Lett 58:1490–1493. doi:10.1103/PhysRevLett.58.1490
Hix WR, Messer OE, Mezzacappa A, Liebendörfer M, Sampaio J, Langanke K, Dean DJ, Martínez-Pinedo G (2003) Consequences of nuclear electron capture in core collapse supernovae. Phys Rev Lett 91(20):201102. doi:10.1103/PhysRevLett.91.201102. astro-ph/0310883

Hoffman RD, Woosley SE, Qian YZ (1997) Nucleosynthesis in neutrino-driven winds. II. Implications for heavy element synthesis. Astrophys J 482:951–962. astro-ph/9611097
Horiuchi S, Beacom JF, Dwek E (2009) Diffuse supernova neutrino background is detectable in super-kamiokande. Phys Rev D 79(8):083013. doi:10.1103/PhysRevD.79.083013. 0812.3157
Horowitz CJ, Pérez-García MA (2003) Realistic neutrino opacities for supernova simulations with correlations and weak magnetism. Phys Rev C 68(2):025803. doi:10.1103/PhysRevC.68.025803. arXiv:astro-ph/0305138
Hüdepohl L, Müller, B, Janka HT, Marek A, Raffelt GGL (2010) Neutrino signal of electron-capture supernovae from core collapse to cooling. Phys Rev Lett 104(25):251,101–+. doi:10.1103/PhysRevLett.104.251101
Janka HT, Hillebrandt W (1989) Monte Carlo simulations of neutrino transport in type II supernovae. Astron Astrophys Suppl 78:375–397
Keil MT, Raffelt GG, Janka HT (2003) Monte Carlo study of supernova neutrino spectra formation. Astrophys J 590:971–991. doi:10.1086/375130. arXiv:astro-ph/0208035
Keil W, Janka HT (1995) Hadronic phase transitions at supranuclear densities and the delayed collapse of newly formed neutron stars. Astron Astrophys 296:145–+
Keil W, Janka HT, Raffelt G (1995) Reduced neutrino opacities and the SN 1987A signal. Phys Rev D 51:6635–6646
Keil W, Janka HT, Schramm DN, Sigl G, Turner MS, Ellis J (1997) Fresh look at axions and SN 1987A. Phys Rev D 56:2419–2432. doi:10.1103/PhysRevD.56.2419. arXiv:astro-ph/9612222
Kunkel W, Madore B, Shelton I, Duhalde O, Bateson FM, Jones A, Moreno B, Walker S, Garradd G, Warner B, Menzies J (1987) Supernova 1987A in the large magellanic cloud. IAU Circ 4316:1
Lattimer JM, Douglas Swesty F (1991) A generalized equation of state for hot, dense matter. Nucl Phys A 535:331–376. doi:10.1016/0375-9474(91)90452-C
Lindquist RW (1966) Relativistic transport theory. Ann Phys 37:487–518. doi:10.1016/0003-4916(66)90207-7
Loredo TJ, Lamb DQ (2002) Bayesian analysis of neutrinos observed from supernova SN 1987A. Phys Rev D 65(6):063,002–+. doi:10.1103/PhysRevD.65.063002
Martínez-Pinedo G, Fischer T, Lohs A, Huther L (2012) Charged-current weak interaction processes in hot and dense matter and its impact on the spectra of neutrinos emitted from proto-neutron star cooling. ArXiv e-prints 1205.2793
Mirizzi A, Tamborra I, Janka HT, Saviano N, Scholberg K, Bollig R, Hudepohl L, Chakraborty S (2015) Supernova neutrinos: production, oscillations and detection. ArXiv e-prints 1508.00785
Nakazato K, Sumiyoshi K, Suzuki H, Totani T, Umeda H, Yamada S (2013) Supernova neutrino light curves and spectra for various progenitor stars: from core collapse to proto-neutron star cooling. Astrophys J Suppl 205:2. doi:10.1088/0067-0049/205/1/2. 1210.6841
Nakazato K, Mochida E, Niino Y, Suzuki H (2015) Spectrum of the supernova relic neutrino background and metallicity evolution of galaxies. Astrophys J 804:75. doi:10.1088/0004-637X/804/1/75. 1503.01236
Ozel F, Psaltis D, Guver T, Baym G, Heinke C, Guillot S (2015) The dense matter equation of state from neutron star radius and mass measurements. Submitted to Astrophys J 1505.05155
Pons JA, Reddy S, Prakash M, Lattimer JM, Miralles JA (1999) Evolution of proto-neutron stars. Astrophys J 513:780–804. doi:10.1086/306889
Pons JA, Reddy S, Ellis PJ, Prakash M, Lattimer JM (2000) Kaon condensation in proto-neutron star matter. Phys Rev C 62(3):035,803–+. doi:10.1103/PhysRevC.62.035803
Pons JA, Miralles JA, Prakash M, Lattimer JM (2001a) Evolution of proto-neutron stars with Kaon condensates. Astrophys J 553:382–393. doi:10.1086/320642
Pons JA, Steiner AW, Prakash M, Lattimer JM (2001b) Evolution of proto-neutron stars with quarks. Phys Rev Lett 86:5223–5226. doi:10.1103/PhysRevLett.86.5223
Prakash M, Bombaci I, Prakash M, Ellis PJ, Lattimer JM, Knorren R (1997) Composition and structure of protoneutron stars. Phys Rep 280:1–77. doi:10.1016/S0370-1573(96)00023-3
Qian YZ, Woosley SE (1996) Nucleosynthesis in neutrino-driven winds. I. The physical conditions. Astrophys J 471:331. doi:10.1086/177973. arXiv:astro-ph/9611094

Raffelt GG (1996) Stars as laboratories for fundamental physics: the astrophysics of neutrinos, axions, and other weakly interacting particles. University of Chicago Press, Chicago
Raffelt GG (2001) Mu- and Tau-neutrino spectra formation in supernovae. Astrophys J 561: 890–914. doi:10.1086/323379. astro-ph/0105250
Reddy S, Prakash M, Lattimer JM (1998) Neutrino interactions in hot and dense matter. Phys Rev D 58(1):013009. doi:10.1103/PhysRevD.58.013009. arXiv:astro-ph/9710115
Reddy S et al (1999) Effects of strong and electromagnetic correlations on neutrino interactions in dense matter. Phys Rev C 59:2888–2918. doi:10.1103/PhysRevC.59.2888
Roberts LF (2012) A new code for proto-neutron star evolution. ArXiv e-prints 1205.3228
Roberts LF, Woosley SE, Hoffman RD (2010) Integrated nucleosynthesis in neutrino-driven winds. Astrophys J 722:954–967. doi:10.1088/0004-637X/722/1/954. 1004.4916
Roberts LF, Reddy S, Shen G (2012) Medium modification of the charged-current neutrino opacity and its implications. Phys Rev C 86(6):065803. doi:10.1103/PhysRevC.86.065803. 1205.4066
Roberts LF, Shen G, Cirigliano V, Pons JA, Reddy S, Woosley SE (2012) Protoneutron star cooling with convection: the effect of the symmetry energy. Phys Rev Lett 108:061,103. doi:10.1103/PhysRevLett.108.061103.
Rrapaj E, Roggero A, Holt JW (2015) Mean field extrapolations of microscopic nuclear equations of state. Submitted to Phys Rev C 1510.00444
Scholberg K (2012) Supernova neutrino detection. Ann Rev Nucl Part Sci 62:81–103. doi:10.1146/annurev-nucl-102711-095006. 1205.6003
Steiner AW, Prakash M, Lattimer JM (2001) Diffusion of neutrinos in proto-neutron star matter with quarks. Phys Lett B 509:10–18. doi:10.1016/S0370-2693(01)00434-8. astro-ph/0101566
Steiner AW, Lattimer JM, Brown EF (2013) The neutron star mass-radius relation and the equation of state of dense matter. Astrophys J Lett 765:L5. doi:10.1088/2041-8205/765/1/L5. 1205.6871
Sumiyoshi K, Suzuki H, Toki H (1995) Influence of the symmetry energy on the birth of neutron stars and supernova neutrinos. Astron Astrophys 303:475. arXiv:astro-ph/9506024
Tews I, Krüger T, Hebeler K, Schwenk A (2013) Neutron matter at next-to-next-to-next-to-leading order in chiral effective field theory. Phys Rev Lett 110(3):032,504. doi:10.1103/PhysRevLett.110.032504. 1206.0025
Thorne KS (1981) Relativistic radiative transfer – moment formalisms. Mon Not R Astro Soc 194:439–473
Wilson JR, Mayle RW (1988) Convection in core collapse supernovae. Phys Rep 163:63–77. doi:10.1016/0370-1573(88)90036-1
Woosley SE, Weaver TA (1995) The evolution and explosion of massive stars. II. Explosive hydrodynamics and nucleosynthesis. Astrophys J Suppl 101:181. doi:10.1086/192237
Woosley SE, Hartmann DH, Hoffman RD, Haxton WC (1990) The nu-process. Astrophys J 356:272–301. doi:10.1086/168839
Woosley SE, Wilson JR, Mathews GJ, Hoffman RD, Meyer BS (1994) The r-process and neutrino-heated supernova ejecta. Astrophys J 433:229–246. doi:10.1086/174638
Woosley SE, Heger A, Weaver TA (2002) The evolution and explosion of massive stars. Rev Modern Phys 74:1015–1071. doi:10.1103/RevModPhys.74.1015